applied sciences

MDPI

Article

Thermal Analysis and Flame-Retarded Mechanism of Composites Composed of Ethylene Vinyl Acetate and Layered Double Hydroxides Containing Transition Metals (Mn, Co, Cu, Zn)

Lili Wang [1,2], Milin Zhang [1] and Bin Li [2,*]

[1] College of Material Science and Chemical Engineering, Harbin Engineering University, Harbin 150001, China; liliwangsh@gmail.com (L.W.); milinzhang@163.com (M.Z.)
[2] College of Science, Northeast Forestry University, Harbin 150040, China
* Correspondence: rainkiss1014@163.com; Tel.: +86-451-8219-2699

Academic Editor: Giorgio Biasiol
Received: 2 April 2016; Accepted: 27 April 2016; Published: 4 May 2016

Abstract: The effects of transition metals on the hydrophobicity of nano–structured layered double hydroxides (LDHs) and the compatibility of LDHs/ethylene vinyl acetate (EVA) composites have seldom been reported. NiMgAl–LDHs slightly surface–modified with stearate and doped with transition metal cations (Mn^{2+}, Co^{2+}, Cu^{2+}, Zn^{2+}) are investigated. Compared to the pure EVA, not only were the maximal degradation–rate temperatures (T_{max}) of the ethylene–based chains enhanced, but also the smoke production rate (SPR) and the production rate of CO (COP) were sharply decreased for all the composites. Most importantly, a new flame retardant mechanism was found, namely the peak heat release rate (pk-HRR) time, which directly depends on the peak production rate of CO_2 (pk-CO_2) time for EVA and all composites by cone calorimeter test. Moreover, the Mn–doped LDH S–NiMgAl–Mn shows more uniform dispersion and better interfacial compatibility in the EVA matrix. The cone calorimetric residue of S–NiMgAl–Mn/EVA has the intumescent char layer and the compact metal oxide layer. Therefore, S–NiMgAl–Mn/EVA shows the lowest pk-HRR and the longest pk-HRR time among all the composites.

Keywords: transition metals; interfacial compatibility; layered double hydroxides; ethylene vinyl acetate copolymer; flame retardancy; thermal stability

1. Introduction

The ethylene vinyl acetate (EVA) copolymer is an important thermoplastic elastomer used in many fields, such as wires, cables, wrappers, encapsulations, adhesive and the drug industries [1–6]. However, EVA is particularly flammable and its subsequent combustion emits toxic smoke CO which limits its application in numerous fields. Therefore, flame retardancy and smoke suppression become an important requirement for EVA [7–10]. Layered double hydroxides (LDHs) are a kind of layered materials that consist of positively charged layers and the interlayer anions. Their general formula can be represented as $[M^{2+}_{1-x}M^{3+}_{x}(OH)_2]^{x+}[A^{n-}]_{x/n}\cdot mH_2O$, where M^{2+} and M^{3+} are divalent and trivalent metal cations, x is the $M^{3+}/(M^{2+}+M^{3+})$ molar ratio and A^{n-} is an n–valent interlayer anion [11–14]. In recent years, LDHs as EVA copolymer halogen–free flame retardants and thermal stabilizers are a rather promising application due to the highly tuneable properties of structure [15–17]. It is well known that homogeneous dispersion and good compatibility of LDHs with polymer matrices contribute to improving the flame retardancy and thermal stability of LDHs/polymer composites [18,19]. Therefore, most studies to date have concentrated on the LDHs of intercalated modification with organic modifier [20,21]. However, although organo–modified

treatment can enhance the hydrophobicity of LDHs, the use of large amounts of organic modifiers is not only detrimental to the flame retardancy of LDHs/polymer composites due to the existence of large amounts of carbon, but is also not environment–friendly. Therefore, a small amount of organic modifier combined with other effective ways to improve the hydrophobicity of LDHs is expected.

In our earlier research, NiMgAl–LDHs clearly showed higher flame retardant efficiency in comparison with MgAl–LDHs in the EVA matrix [22,23]. Furthermore, we explored NiMgAl–LDHs with rare earth ions to improve the hydrophobicity of LDHs. The result indicated that La or Ce evidently enhance the flame retardancy and mechanical properties of LDHs/EVA composites. However, the rare earth is especially rare and precious. It has an impact on the industrial application of materials containing rare earth [24]. In addition, CO_2 from the interlayer carbonate of LDHs can contribute to isolating oxygen during combustion [25]. Therefore, in the present study, NiMgAl–LDHs containing carbonate slightly surface–modified with sodium stearate and doped with inexpensive transition metal cations (Mn^{2+}, Co^{2+}, Cu^{2+}, Zn^{2+}) were synthesized. This study mainly focuses on the effects of the transition metal ions on the crystallinity, morphology, thermal property and hydrophobicity of the LDHs. Moreover, the influences of the transition metals on the thermal properties and flame retardancy of LDHs/EVA composites are also investigated.

2. Materials and Methods

2.1. Materials

All chemicals used in the preparation are analytical grade without further purification. Nickel nitrate (99%), aluminum nitrate (99%), magnesium nitrate (99%), manganese nitrate (99%), cobalt nitrate (99%), copper nitrate (99%), zinc nitrate (99%), sodium stearate (99%), sodium carbonate (99%) and sodium hydroxide (99%) were purchased from Tianjin Kemiou Fine Chemical Reagent Co. (Tianjin, China). EVA (VA-28%) was offered from Samsung Co. (Seoul, Korea). Deionized water was made by a Milli-Q pure water apparatus in our Lab.

2.2. Synthesis of the Stearate Modified NiMgAl–LDHs with Transition Metal

In a four–necked flask (l L), a mixed aqueous solution containing 1 M transition metal nitrate, 1 M $Ni(NO_3)_2$, 1 M $Mg(NO_3)_2$ and 1 M $Al(NO_3)_3$, with a molar ratio of transition metal cations: Ni^{2+}:Mg^{2+}:Al^{3+} of 0.5:0.5:2:1, was added dropwise to 100 mL of deionized water at 70 °C under continuous magnetic stirring, while the pH was adjusted to 8–9 by adding a NaOH–Na_2CO_3 mixed solution (0.6 M NaOH and 0.45 M Na_2CO_3). After the titration, a heavy gel suspension was obtained, which was crystallized at 70 °C for 30 min in a microwave oven (XH–300A, 1000 W, 2.45 GHz). The precipitate was washed with deionized water to pH 7 and then filtered. The synthesized sample was dried in air at 70 °C.

Sodium stearate (0.15 g) and the above synthesized LDHs precursors (10 g) were dispersed into 200 mL deionized water. The mixture was vigorously stirred at 70 °C with microwave irradiation for 30 min. The precipitate was then washed to pH 7 with 70 °C hot water to eliminate the excess sodium stearate. Finally, the precipitate was filtered and dried. The resulting surface modified LDHs were named S–NiMgAl–Mn, S–NiMgAl–Co, S–NiMgAl–Cu and S–NiMgAl–Zn, respectively.

2.3. Preparation of LDHs/EVA Composites

The LDHs/EVA composites containing 20 wt. % LDHs were prepared via melt blending at 140 °C in an RM–200A torque rheometer for 10 min with a rotor speed of 60 rpm. These synthesized composites were named S–NiMgAl–Mn/EVA, S–NiMgAl–Co/EVA, S–NiMgAl–Cu/EVA and S–NiMgAl–Zn/EVA, respectively.

2.4. Measurements

X–ray diffraction (XRD) data were collected using a D/MAX 2200 diffractometer (Rigaku, Tokyo, Japan) with Cu Kα irradiation operated at 40 kV and 45 mA. The samples were scanned in the 2θ

range of 5 to 75° and step size of 0.02° at 4 s for each step. Fourier transform infrared spectra (FTIR) were collected using a Nicolet FTIR360 spectrometer (Thermo Nicolet, Madison, WI, USA) (KBr pellet method, 4 cm^{-1} resolution, number of scans is 32 times). Scanning electron microscope (SEM) observations of LDHs, LDHs/EVA composites and the cone calorimetric residue were conducted on an FEI–Sirion instrument (FEI, Eindhoven, the Netherlands) with a field emission of 20 kV. The specimens were examined in a HITACHI 1H–7650 transmission electron microscope (TEM) (Hitachi, Tokyo, Japan) operated at an accelerating voltage of 100 kV. Contact angles were measured using a JC2000A contact angle and interface tensile measurer (Shanghai photoelectric, Shanghai, China). Samples were pressed into disks with a diameter of 11 mm and thickness of 0.4 mm. Deionized water (3 μL) was dripped onto each disk, and the drops were observed for 30 s. Each measurement was repeated five times. Thermogravimetric (TGA) and differential thermogravimetry (DTG) analyses were conducted using a Perkin Elmer Pyris 1 Thermal Analyzer (Perkin Elmer, Norwalk, CT, USA) at a linear heating rate of 10 °C/min in pure nitrogen from 50 °C to 800 °C, using a sample mass of 3 to 4 mg. Calorimetry tests were conducted in a cone calorimeter at an incident heat flux of 50 kW/m^2 according to the ISO 5660–1 standard. The polymer sample (100 × 100 × 5 mm^3) was placed horizontally on the balance holder.

3. Results and Discussion

3.1. XRD, FTIR and Morphology Analysis of LDHs

The XRD patterns of S–NiMgAl–Mn, S–NiMgAl–Co, S–NiMgAl–Cu and S–NiMgAl–Zn are shown in Figure 1a–d, respectively. All patterns exhibit the (003), (006), (012), (015), (018), (110) and (113) characteristic reflections of the LDHs structure [26,27]. From the intensity of the main reflections (003) and (006), one can find that under the same reaction conditions, the Mn– and Zn–doped LDHs have higher crystallinity than those containing Co and Cu [28,29]. The basal spacing (d_{basal}) of S–NiMgAl–Mn, S–NiMgAl–Co, S–NiMgAl–Cu and S–NiMgAl–Zn were calculated from the (003) reflection, are 7.76, 7.81, 7.82 and 7.73 Å, respectively. These values confirm that the interlayers of the four LDHs exist with CO_3^{2-}, but do not coexist with NO_3^- or $C_{18}H_{35}O_2^-$ [30,31]. Furthermore, FTIR spectra of LDHs are shown in Figure 2A. The bands at 1369 cm^{-1} also confirm that the interlayer anions of all LDHs are CO_3^{2-} without the coexistence of NO_3^- (at 1384 cm^{-1}) [32–34]. The bands at 867 and 665 cm^{-1} are characteristic of carbonate for the ν_2 (out-of-plane deformation) and the ν_4 (in-plane bending) vibrations, respectively [35]. Meanwhile, the bands at 1484 and 1426 cm^{-1} are assigned to the bridged bidentate complexation of interlayer CO_3^{2-}–CO_3^{2-} in the LDHs [36]. Note that the bands at 1484 and 1426 cm^{-1} disappear in S–NiMgAl–Mn due to the existence of Mn^{2+}.

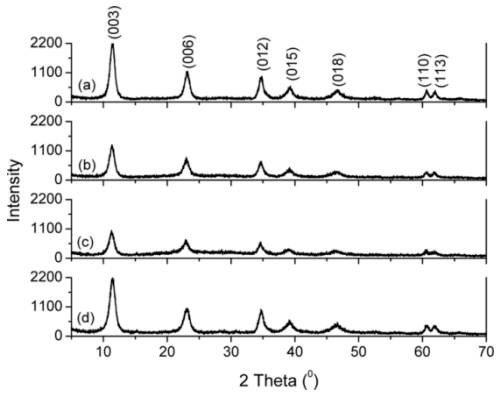

Figure 1. XRD (X-Ray diffraction) patterns of the synthesized layered double hydroxides (LDHs). (**a**) S–NiMgAl–Mn; (**b**) S–NiMgAl–Co; (**c**) S–NiMgAl–Cu and (**d**) S–NiMgAl–Zn.

The broad and intense FTIR absorption band at 3460 cm^{-1} is attributed to the O–H stretching vibrations of layered hydroxyl groups and interlayer water molecules [37]. The bands at 1634 cm^{-1} can be assigned to the bending vibration of interlayer water molecules [38]. The bands at 786 and 427 cm^{-1} are ascribed to $[AlO_6]^{3-}$ condensed groups and the deformation of M–OH in the brucite–like layers, respectively [39,40]. Furthermore, all LDHs also display bands at 2956, 2922 and 2852 cm^{-1}, which are associated with the C–H stretching vibrations of stearate. In addition, the antisymmetric stretching vibration of the carbonyl group from 1560 cm^{-1} of pure stearate is shifted to 1545 cm^{-1} due to the layer hydroxyl groups hydrogen–bonded to carbonyl group of stearate anions [30,41,42]. Therefore, the combined analysis of FTIR and XRD confirms that the stearate is successfully grafted on the surface of LDHs. Figure 2B shows the schematic illustration of stearate surface modified LDHs. Moreover, it is worth mentioning that the weak shoulder at 1545 cm^{-1} is not detected for S–NiMgAl–Zn. This fact indicates that the grafted amount of stearate was least for S–NiMgAl–Zn. In contrast, the grafted amount of stearate was the most for S–NiMgAl–Mn. The grafted amount of stearate can be further confirmed by morphological studies of LDHs.

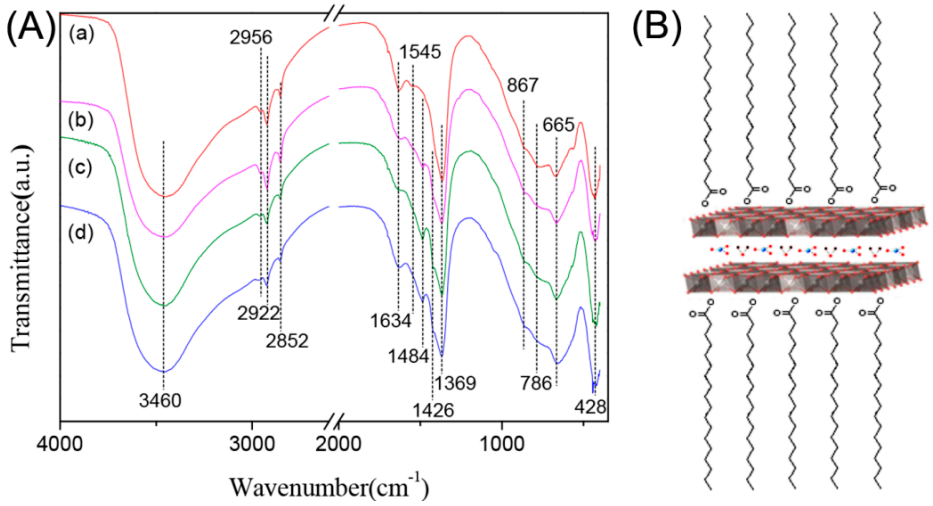

Figure 2. (**A**) FTIR (Fourier transform infrared spectroscopy) spectra of the synthesized LDHs. (**a**) S–NiMgAl–Mn; (**b**) S–NiMgAl–Co; (**c**) S–NiMgAl–Cu and (**d**) S–NiMgAl–Zn; (**B**) Schematic illustration of stearate surface modified LDHs.

3.2. Morphology and Contact Angle Analysis of the LDHs

Figure 3A illustrates the SEM images for the four LDHs. S–NiMgAl–Mn and S–NiMgAl–Co show better effect of grafting for the stearate. In particular, the surface of S–NiMgAl–Mn was uniformly coated by the stearate. Therefore, S–NiMgAl–Mn can be expected to show better compatibility with the EVA matrix. However, the unmodified particles of many petal–like structures for S–NiMgAl–Zn can be seen clearly. This result indicates that S–NiMgAl–Zn has the least grafted amount of stearate. This result is consistent with that of the IR analysis. In addition, TEM images show flake particle morphology and crystal sizes of nanometre thickness (as shown in Figure 3B).

The contact angles were measured to investigate the influences of metal cations (Mn^{2+}, Co^{2+}, Cu^{2+} and Zn^{2+}) on the hydrophobicity of LDHs (as shown in Figure 4). The contact angle values for S–NiMgAl–Mn, S–NiMgAl–Co, S–NiMgAl–Cu and S–NiMgAl–Zn are 92°, 83°, 68° and 88°, respectively. S–NiMgAl–Mn has the largest contact angle. One possible reason is that S–NiMgAl–Mn has better grafting effect of the stearate than the other three LDHs. However, note that although S–NiMgAl–Zn has the least stearate, the hydrophobicity of S–NiMgAl–Zn is greater than those of S–NiMgAl–Co and S–NiMgAl–Cu. This indicates that the inherent nature of different transition metal ions has an important role in the hydrophobicity of LDHs.

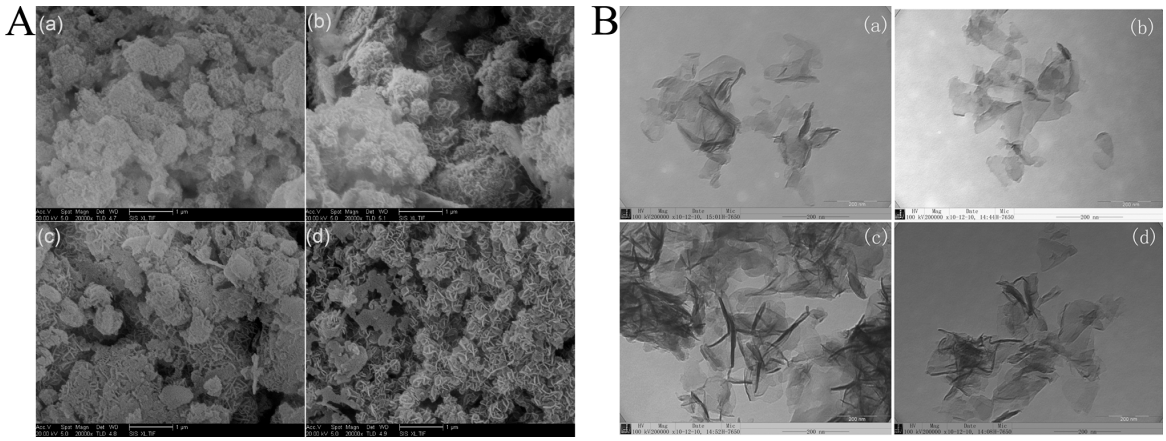

Figure 3. A: SEM (20000×) and **B:** TEM images (200000×) of the synthesized LDHs. (**a**) S–NiMgAl–Mn; (**b**) S–NiMgAl–Co; (**c**) S–NiMgAl–Cu and (**d**) S–NiMgAl–Zn.

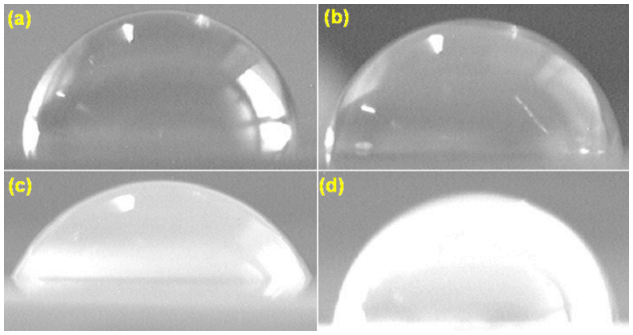

Figure 4. Contact angle images of the synthesized LDHs. (**a**) S–NiMgAl–Mn; (**b**) S–NiMgAl–Co; (**c**) S–NiMgAl–Cu and (**d**) S–NiMgAl–Zn.

3.3. Thermal Analysis of the LDHs

Figure 5A,B illustrate the TGA and DTG curves for four LDHs, respectively. Upon heating, all LDHs mainly underwent two stages of decomposition. The mass loss of absorbed water and interlayer water in the TGA curve (50 ~ 200 °C) for S–NiMgAl–Mn, S–NiMgAl–Co, S–NiMgAl–Cu and S–NiMgAl–Zn are 15.5%, 14.9%, 13.5% and 14.3%, respectively. From the DTG curves, it can be seen that the maximal degradation–rate temperature (T_{max}) of water molecules for S–NiMgAl–Mn, S–NiMgAl–Co, S–NiMgAl–Cu and S–NiMgAl–Zn are 188 °C, 178 °C, 174 °C and 181 °C, respectively. The second stage of decomposition, occurring at a higher temperature (200 ~ 800 °C), is associated with the dehydroxylation of the metal hydroxide layers and the degradation of carbonates and stearate in the LDHs. From the TGA curves, it can be seen that the mass losses of hydroxyls, carbonates and stearate for S–NiMgAl–Mn, S–NiMgAl–Co, S–NiMgAl–Cu and S–NiMgAl–Zn are 28.0%, 30.1%, 30.4% and 29.9%, respectively. The T_{max} of hydroxyls and carbonates is about 330 °C for all LDHs in the DTG curves.

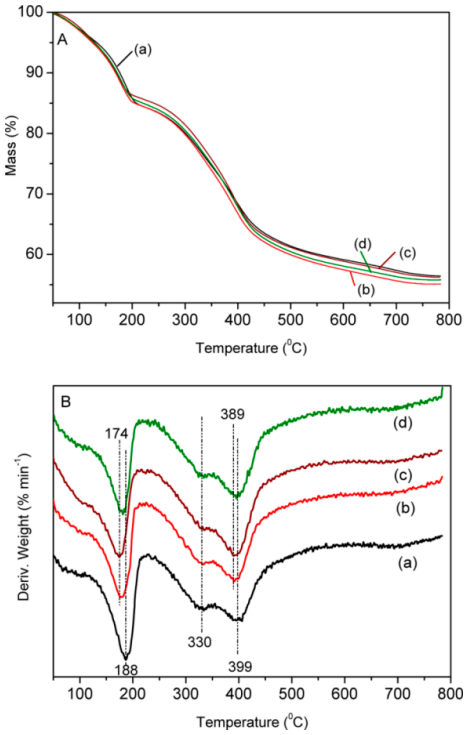

Figure 5. A: Thermogravimetric analysis (TGA) and **B**: differential thermogravimetry (DTG) curves of the synthesized LDHs. (**a**) S–NiMgAl–Mn; (**b**) S–NiMgAl–Co; (**c**) S–NiMgAl–Cu and (**d**) S–NiMgAl–Zn.

3.4. Thermal Analysis and Flame Retardancy of EVA and its Composites

Figure 6 illustrates the TGA and DTG curves of EVA and its composites with 20 wt. % loading of LDHs. The mass loss of EVA shows two degradation steps in the temperature range from 307 to 550 °C. The first one is attributed to the deacetylation of acetate side groups. The second one is due to the degradation of polyethylene chains at high temperatures [43]. However, all of the composites display three mass loss steps. The first step corresponds to the removal of the interlayer water molecules, dehydroxylation and decomposition of the interlayer anions in the range of 120 to 307 °C [14]. From the DTG curves, it can be seen that the T_{max} of the acetate side groups for all of the composites occurs at 383 °C, that of the ethylene–based chains is at 496 °C for S–NiMgAl–Co/EVA, S–NiMgAl–Cu/EVA and S–NiMgAl–Zn/EVA, while that of S–NiMgAl–Mn/EVA is at 503 °C. These values are higher than that of the EVA (484 °C) and the earlier reported undoped transition metal composite NiMgAl–LDH/EVA (493 °C) [22].

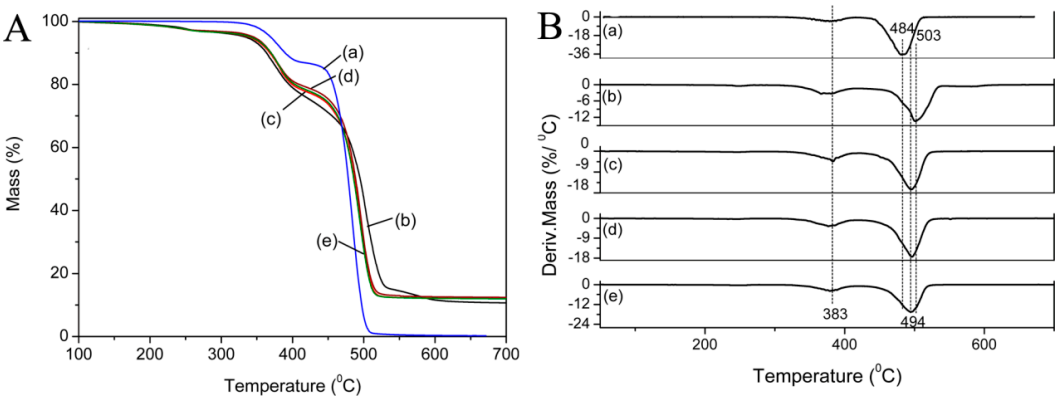

Figure 6. A: TGA and **B**: DTG curves for ethylene vinyl acetate (EVA) and composites. (**a**) EVA; (**b**) S–NiMgAl–Mn/EVA; (**c**) S–NiMgAl–Co/EVA; (**d**) S–NiMgAl–Cu/EVA and (**e**) S–NiMgAl–Zn/EVA.

Cone calorimeter test is used to predict the combustion behavior of materials in real fire scenarios [44]. Figure 7a–d present the heat release rate (HRR), the total heat release (THR), the smoke production rate (SPR) and the production rate of CO (COP) curves of the pure EVA and its composites, respectively. Table 1 lists the corresponding combustion data. From Table 1 and Figure 7a, it can be seen that the peak heat release rate (pk-HRR) of EVA, S–NiMgAl–Mn/EVA, S–NiMgAl–Co/EVA, S–NiMgAl–Cu/EVA and S–NiMgAl–Zn/EVA are 1247, 445, 467, 451 and 485 kW/m^2, respectively. The reductions in pk–HRR for all of the composites are 61% greater than that of EVA. In addition, the pk-HRR time for EVA, S–NiMgAl–Mn/EVA, S–NiMgAl–Co/EVA, S–NiMgAl–Cu/EVA and S–NiMgAl–Zn/EVA are 315, 466, 429, 170 and 149 s, respectively. S–NiMgAl–Mn/EVA shows the lowest pk-HRR and the longest pk-HRR time among all samples. At the same time, compared with the ignition time (T_{ign}) of the EVA of 62 s, the T_{ign} of S–NiMgAl–Mn/EVA, S–NiMgAl–Cu/EVA and S–NiMgAl–Zn/EVA are postponed to 74, 82 and 66 s, respectively. In contrast, T_{ign} of S–NiMgAl–Co/EVA was shortened to 58 s. Therefore, S–NiMgAl–Cu/EVA is the most difficult material to burn for longer T_{ign}. The fire performance index (FPI) is another important fire resistance parameter. FPI is defined as the ratio of pk–HRR to T_{ign}. The FPI values of S–NiMgAl–Mn/EVA, S–NiMgAl–Co/EVA, S–NiMgAl–Cu/EVA and S–NiMgAl–Zn/EVA are 6, 8, 6 and 7 kW/m^{2}s, respectively. These values are much smaller than that of the EVA (20 kW/m^{2}s), confirming that S–NiMgAl–Mn/EVA and S–NiMgAl–Cu/EVA have better flame retardant efficiency. In addition, the THR values for all the composites are slightly decreased compared with that of the EVA.

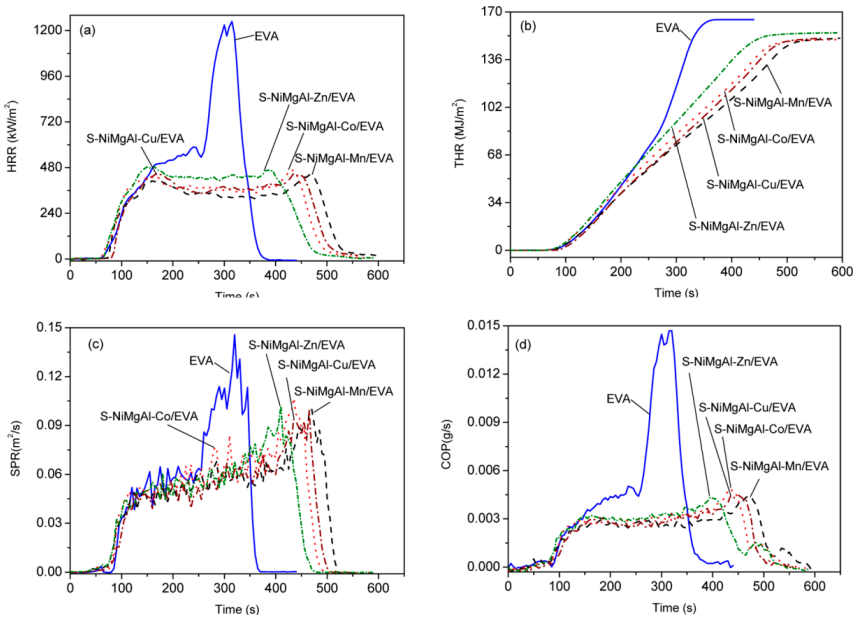

Figure 7. Cone calorimetry results of EVA and its composites with 20 wt. % LDHs. (**a**) Heat release rate (HRR) curves; (**b**) total heat release (THR) curves; (**c**) smoke production rate (SPR) curves and (**d**) production rate of CO (COP) curves.

Table 1. Cone calorimetry data for composites with 20 wt. % loading of stearate surface-modified LDHs containing transition metal elements (heat flux of 50 kW/m^2).

Samples	pk-HRR (kW/m^2)	Reduction (%)	Tign (s)	FPI (kW/m^{2}s)	THR (MJ/m^2)	pk-SPR (m^2/s)	pk-COP (g/s)
EVA	1247	-	62	20	164	0.146	0.0147
S-NiMgAl-Mn/EVA	445	64.3	74	6	151	0.100	0.0044
S-NiMgAl-Co/EVA	467	62.6	58	8	150	0.107	0.0049
S-NiMgAl-Cu/EVA	451	63.8	82	6	151	0.0997	0.0045
S-NiMgAl-Zn/EVA	485	61.1	66	7	155	0.102	0.0044

It is well known that most injuries and deaths result from the smoke and toxic gases in the case of fire. The peak smoke production rate (pk–SPR) for EVA, S–NiMgAl–Mn/EVA, S–NiMgAl–Co/EVA, S–NiMgAl–Cu/EVA and S–NiMgAl–Zn/EVA are 0.146, 0.100, 0.107, 0.0997 and 0.102 m^2/s, respectively. Furthermore, peak production rate of CO (pk–COP) are 0.0147, 0.0044, 0.0049, 0.0045 and 0.0044 g/s for EVA, S–NiMgAl–Mn/EVA, S–NiMgAl–Co/EVA, S–NiMgAl–Cu/EVA and S–NiMgAl–Zn/EVA, respectively. The pk–SPR and pk–COP for all the composites decrease significantly compared to EVA as listed in Table 1. In addition, MCOY is the mean release yield of CO of burning materials. The MCOY values of EVA, S–NiMgAl–Mn/EVA, S–NiMgAl–Co/EVA, S–NiMgAl–Cu/EVA and S–NiMgAl–Zn/EVA are 0.0362, 0.0277, 0.0281, 0.0268 and 0.0271 kg/kg, respectively. Compared to the EVA, MCOY values for composites show an evident decrease. In particular, S–NiMgAl–Cu/EVA has the smallest MCOY value among all the composites. The above conecalorimeter data provide evidence that the composites show important improvement of both the flame retardancy and the smoke/toxic gas suppression, especially for S–NiMgAl–Mn/EVA.

3.5. Flame Retardant Mechanism

The S–NiMgAl–Mn contains more water molecules, which can help to improve the flame retardancy and the thermal stability of S–NiMgAl–Mn/EVA. However, the released temperatures of H_2O and CO_2 for S–NiMgAl–Mn are higher than other composites, which in turn is adverse for the enhancement of the flame retardancy and the thermal stability of S–NiMgAl–Mn/EVA. In order to determine the interfacial compatibility of LDHs particles in the EVA matrix, Figure 8 shows the SEM micrographs of fracture surfaces for all composites. The fracture surface of S–NiMgAl–Cu/EVA is ductile, while the other three composites undergo brittle fracture under liquid nitrogen freezing conditions. Furthermore, note that the interface between EVA and S–NiMgAl–Mn is the smoothest. This result indicates that S–NiMgAl–Mn has more uniform dispersion, as well as the best interfacial compatibility with the EVA matrix. However, the particles of S–NiMgAl–Co and S–NiMgAl–Zn appear more aggregated in the EVA matrix, which leads to relatively poor interfacial compatibility. Therefore, the homogeneous dispersion and the good compatibility of S–NiMgAl–Mn with the EVA matrix contribute better to the property improvement of S–NiMgAl–Mn/EVA.

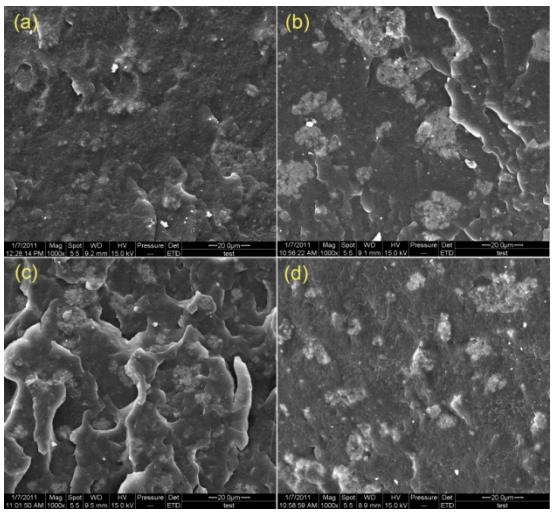

Figure 8. SEM images (1000×) of fractured surfaces for all the composites with 20 wt. % LDH. (**a**) S–NiMgAl–Mn/EVA; (**b**) S–NiMgAl–Co/EVA; (**c**) S–NiMgAl–Cu/EVA and (**d**) S–NiMgAl–Zn/EVA.

Figure 9 illustrate SEM micrographs of the cone calorimetric residue for the composites S–NiMgAl–Mn/EVA, S–NiMgAl–Co/EVA, S–NiMgAl–Cu/EVA and S–NiMgAl–Zn/EVA, respectively. It is worth noting that the surface of residue for S–NiMgAl–Mn/EVA and S–NiMgAl–Cu/EVA have the intumescent char layer. In particular, the compact metal oxide

layer of residue surface for S–NiMgAl–Mn/EVA can more effectively prevent the diffusion of heat and oxygen. In contrast, the residues of S–NiMgAl–Co/EVA and S–NiMgAl–Zn/EVA have no intumescent char layer or compact metal oxide layer. Meanwhile, there are many small holes on the surface of the loose inorganic residue of S–NiMgAl–Zn/EVA. Thus, heat and flammable volatiles could easily penetrate into the flame zone during the burning process of S–NiMgAl–Zn/EVA.

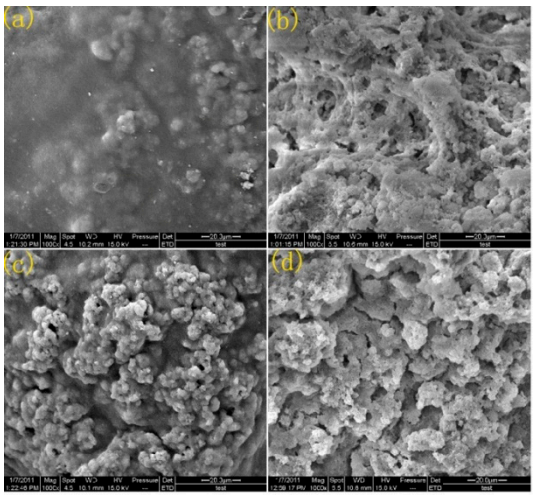

Figure 9. SEM micrographs (1000×) of the cone calorimetric residue for the composites, (**a**): S–NiMgAl–Mn/EVA; (**b**): S–NiMgAl–Co/EVA; (**c**): S–NiMgAl–Cu/EVA and (**d**): S–NiMgAl–Zn/EVA.

In addition, another crucial phenomenon was observed. The shape of production rate of CO_2 (CO_2P) curves (as shown in Figure 10) is same as the HRR curves. The peak production rate of CO_2(pk-CO_2P) time values are 315, 466, 429, 170 and 149 s for EVA, ELDH-0, ELDH-Ni, ELDH-Co and ELDH-Cu, respectively. The pk-CO_2P time is completely the same as the corresponding pk-HRR time. The result reveals that the when the production rate of CO_2 reached to the pk-CO_2P, the HRR of samples simultaneously reached the pk-HRR. Therefore, the pk-HRR time is directly determined by the pk-CO_2 time for EVA and composites.

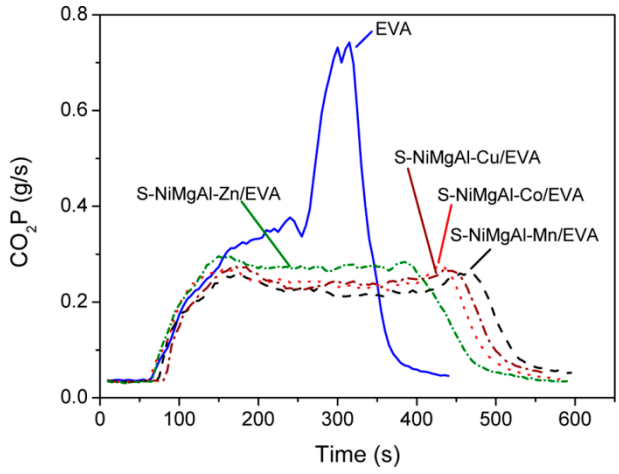

Figure 10. CO_2P curves of EVA and its composites with 20 wt. % LDHs.

4. Conclusions

The different transition metal cations, Mn^{2+}, Co^{2+}, Cu^{2+} and Zn^{2+}, have different influences on the crystallinity, morphology, hydrophobicity and thermal degradation temperature of modified

LDHs. The combination of FTIR and XRD results indicates that a little stearate is grafted on the LDHs surfaces. S–NiMgAl–Mn significantly improves the thermal stability and flame retardancy of S–NiMgAl–Mn/EVA. On one hand, this is due to better interfacial compatibility of S–NiMgAl–Mn with the EVA matrix. On the other hand, the dense char and compact metal oxide layer of combustion residue also contribute to the property improvement of S–NiMgAl–Mn/EVA. Moreover, a new flame retardant mechanism was found, the pk-HRR time directly depends on the pk-CO_2 time of EVA and composites. These synthetic LDHs can be used as good flame retardant and smoke suppression materials of polymer products. Furthermore, because the synthesis process of the non-toxic and inexpensive LDHs is simple, it is feasible to produce them in large quantity and brings favorable economic benefits.

Acknowledgments: This study was financially supported by the China Postdoctoral Science Foundation Special Funding Project (No. 2014T70308) and the National Natural Science Foundation of China (No. 21304014).

Author Contributions: The author Lili Wang contributed research and experimental work in this study. The authors Milin Zhang and Bin Li contributed data analysis work and revision of this paper.

Conflicts of Interest: The authors declare no conflict of interest.

References

1. Thuo, M.M.; Martinez, R.V.; Lan, W.J.; Liu, X.; Barber, J.; Atkinson, M.B.J.; Bandarage, D.; Bloch, J.F.; Whitesides, G.M. Fabrication of low-cost paper-based microfluidic devices by embossing or cut-and-stack methods. *Chem. Mater.* **2014**, *26*, 4230–4237.
2. Sabet, M.; Hassan, A.; Ratnam, C.T. Electron beam irradiation of low density polyethylene/ethylene vinyl acetate filled with metal hydroxides for wire and cable applications. *Polym. Degrad. Stab.* **2012**, *97*, 1432–1437. [CrossRef]
3. Hintersteiner, I.; Sternbauer, L.; Beissmann, S.; Buchberger, W.W.; Wallner, G.M. Determination of stabilisers in polymeric materials used as encapsulants in photovoltaic modules. *Polym. Test.* **2014**, *33*, 172–178. [CrossRef]
4. Goldshtein, J.; Bretler, U.; Lublin-Tennenbaum, T.; Gluz, E.; Margel, S. Solidification of non-halogen fire-retardant liquids by encapsulation within porous uniform PDVB microspheres for preparation of fire-retardant polymeric blends. *Colloid Polym. Sci.* **2014**, *292*, 2241–2248. [CrossRef]
5. He, X.; Zhang, R.; Chen, Q.; Rong, Y.; Yang, Z. Different surface functionalized nano-Fe_3O_4 particles for EVA composite adhesives. *Int. J. Adhes.* **2014**, *50*, 128–135. [CrossRef]
6. Guo, Q.; Guo, S.; Wang, Z. A type of esophageal stent coating composed of one 5–fluorouracil–containing EVA layer and one drug–free protective layer: *In vitro* release, permeation and mechanical properties. *J. Controlled Release* **2007**, *118*, 318–324. [CrossRef] [PubMed]
7. Jiao, C.; Chen, X. Synergistic effects of zinc oxide with layered double hydroxides in EVA/LDH composites. *J. Therm. Anal. Calorim.* **2009**, *98*, 813–818. [CrossRef]
8. Wang, X.; Pang, H.; Chen, W.; Lin, Y.; Zong, L.; Ning, G. Controllable fabrication of zinc borate hierarchical nanostructure on brucite surface for enhanced mechanical properties and flame retardant behaviors. *Acs. Appl. Mater Inter.* **2014**, *6*, 7223–7235. [CrossRef] [PubMed]
9. Lu, K.; Cao, X.; Liang, Q.; Wang, H.; Cui, X.; Li, Y. Formation of a compact protective layer by magnesium hydroxide incorporated with a small amount of intumescent flame retardant: new route to high performance nonhalogen flame retardant TPV. *Ind. Eng. Chem. Res.* **2014**, *53*, 8784–8792. [CrossRef]
10. Wang, B.; Wang, X.; Shi, Y.; Tang, G.; Tang, Q.; Song, L.; Hu, Y. Effect of vinyl acetate content and electron beam irradiation on the flame retardancy, mechanical and thermal properties of intumescent flame retardant ethylene–vinyl acetate copolymer. *Radiat. Phys. Chem.* **2012**, *81*, 308–315. [CrossRef]
11. Theiss, F.L.; Ayoko, G.A.; Frost, R.L. Thermogravimetric analysis of selected layered double hydroxides. *J. Therm. Anal. Calorim.* **2013**, *112*, 649–657. [CrossRef]
12. Xue, X.; Gu, Q.; Pan, G.; Liang, J.; Huang, G.; Sun, G.; Ma, S.; Yang, X. Nanocage structure derived from sulfonated β-cyclodextrin intercalated layered double hydroxides and selective adsorption for phenol compounds. *Inorg. Chem.* **2014**, *53*, 1521–1529. [CrossRef] [PubMed]

13. Wang, G.; Rao, D.; Li, K.; Lin, Y. UV Blocking by Mg–Zn–Al layered double hydroxides for the protection of asphalt road surfaces. *Ind. Eng. Chem. Res.* **2014**, *53*, 4165–4172. [CrossRef]
14. Özgümüş, S.; Gök, M.K.; Bal, A.; Güçlü, G. Study on novel exfoliated polyampholyte nanocomposite hydrogels based on acrylic monomers and Mg–Al–Cl layered double hydroxide: Synthesis and characterization. *Chem. Eng. J.* **2013**, *223*, 277–286. [CrossRef]
15. Li, L.; Qian, Y.; Jiao, C. Synergistic flame retardant effects of ammonium polyphosphate in ethylene-vinyl acetate/layered double hydroxides composites. *Polym. Eng. Sci.* **2014**, *54*, 766–776. [CrossRef]
16. Goodarzi, V.; Jafari, S.H.; Khonakdar, H.A.; Monemian, S.A.; Mortazavi, M. An assessment of the role of morphology in thermal/thermo–oxidative degradation mechanism of PP/EVA/clay nanocomposites. *Polym. Degrad. Stab.* **2010**, *95*, 859–869. [CrossRef]
17. Nyambo, C.; Kandare, E.; Wilkie, C.A. Thermal stability and flammability characteristics of ethylene vinyl acetate (EVA) composites blended with a phenyl phosphonate-intercalated layered double hydroxide (LDH), melamine polyphosphate and/or boric acid. *Polym. Degrad. Stab.* **2009**, *94*, 513–520. [CrossRef]
18. Matusinovic, Z.; Lu, H.; Wilkie, C.A. The role of dispersion of LDH in fire retardancy: The effect of dispersion on fire retardant properties of polystyrene/Ca−Al layered double hydroxide nanocomposites. *Polym. Degrad. Stab.* **2012**, *97*, 1563–1568. [CrossRef]
19. Manzi-Nshuti, C.; Songtipya, P.; Manias, E.; Jimenez-Gasco, M.M.; Hossenlopp, J.M.; Wilkie, C.A. Polymer nanocomposites using zinc aluminum and magnesium aluminum oleate layered double hydroxides: Effects of LDH divalent metals on dispersion, thermal, mechanical and fire performance in various polymers. *Polymer.* **2009**, *50*, 3564–3574. [CrossRef]
20. Ardanuy, M.; Velasco, J.I. Mg–Al layered double hydroxide nanoparticles. *Appl. Clay Sci.* **2011**, *51*, 341–347. [CrossRef]
21. Wang, D.Y.; Leuteritz, A.; Kutlu, B.; Landwehr, M.; Jehnichen, D.; Wagenknecht, U.; Heinrich, G. Preparation and investigation of the combustion behavior of polypropylene/organomodified MgAl–LDH micro–nanocomposite. *J. Alloys Compd.* **2011**, *509*, 3497–3501. [CrossRef]
22. Wang, L.; Li, B.; Yang, M.; Chen, C.; Liu, Y. Effect of Ni cations and microwave hydrothermal treatment on the related properties of layered double hydroxide–ethylene vinyl acetate copolymer composites. *J. Colloid Interface Sci.* **2011**, *356*, 519–525. [CrossRef] [PubMed]
23. Wang, L.; Li, B.; Hu, Z.; Cao, J. Effect of nickel on the properties of composites composed of layered double hydroxides and ethylene vinyl acetate copolymer. *Appl. Clay Sci.* **2013**, *72*, 138–146. [CrossRef]
24. Wang, L.; Li, B.; Zhao, X.; Chen, C.; Cao, J. Effect of rare earth ions on the properties of composites composed of ethylene vinyl acetate copolymer and layered double hydroxides. *PLoS ONE* **2012**, *7*, e37781. [CrossRef] [PubMed]
25. Palmer, S.J.; Frost, R.L. Determination of the mechanism(s) for the inclusion of arsenate, vanadate, or molybdate anions into hydrotalcites with variable cationic ratio. *J. Colloid Interface Sci.* **2009**, *329*, 404–409. [CrossRef] [PubMed]
26. Ramírez-Moreno, M.J.; Romero-Ibarra, I.C.; Hernández-Pérez, M.A.; Pfeiffer, H. CO_2 adsorption at elevated pressure and temperature on Mg–Al layered double hydroxide. *Ind. Eng. Chem. Res.* **2014**, *53*, 8087–8094. [CrossRef]
27. Jabłońska, M.; Chmielarz, L.; Węgrzyn, A.; Guzik, K.; Piwowarska, Z.; Witkowski, S.; Walton, R.I.; Dunne, P.W.; Kovanda, F. Thermal transformations of Cu–Mg (Zn)–Al(Fe) hydrotalcite-like materials into metal oxide systems and their catalytic activity in selective oxidation of ammonia to dinitrogen. *J. Therm. Anal. Calorim.* **2013**, *114*, 731–747. [CrossRef]
28. Benito, P.; Herrero, M.; Labajos, F.M.; Rives, V.; Royo, C.; Latorre, N.; Monzon, A. Production of carbon nanotubes from methane use of Co–Zn–Al catalysts prepared by microwave–assisted synthesis. *Chem. Eng. J.* **2009**, *149*, 455–462. [CrossRef]
29. Benito, P.; Guinea, I.; Labajos, F.M.; Rocha, J.; Rives, V. Microwave–hydrothermally aged Zn, Alhydrotalcite–like compounds: Influence of the composition and the irradiation conditions. *Microporous Mesoporous Mater.* **2008**, *110*, 292–302. [CrossRef]
30. Ishihara, S.; Sahoo, P.; Deguchi, K.; Ohki, S.; Tansho, M.; Shimizu, T.; Labuta, J.; Hill, J.P.; Ariga, K.; Watanabe, K.; *et al.* Dynamic breathing of CO_2 by hydrotalcite. *J. Am. Chem. Soc.* **2013**, *135*, 18040–18043. [CrossRef] [PubMed]

31. Otero, R.; Fernández, J.M.; González, M.A.; Pavlovic, I.; Ulibarri, M.A. Pesticides adsorption–desorption on Mg–Al mixed oxides. Kinetic modeling, competing factors and recyclability. *Chem. Eng. J.* **2013**, *221*, 214–221. [CrossRef]
32. Xue, T.; Gao, Y.; Zhang, Z.; Umar, A.; Yan, X.; Zhang, X.; Guo, Z.; Wang, Q. Adsorption of acid red from dye wastewater by Zn_2Al-NO_3 LDHs and the resource of adsorbent sludge as nanofiller for polypropylene. *J. Alloy. Compd.* **2014**, *587*, 99–104. [CrossRef]
33. Bouariu, S.; Dartu, L.; Carja, G. Silver-layered double hydroxides self-assemblies. *J. Therm. Anal. Calorim.* **2012**, *111*, 1263–1271. [CrossRef]
34. Ma, S.; Shim, Y.; Islam, S.M.; Subrahmanyam, K.S.; Wang, P.; Li, H.; Wang, S.; Yang, X.; Kanatzidis, M.G. Efficient Hg vapor capture with polysulfide intercalated layered double hydroxides. *Chem. Mater.* **2014**, *26*, 5004–5011. [CrossRef]
35. Violante, A.; Pucci, M.; Cozzolino, V.; Zhu, J.; Pigna, M. Sorption/desorption of arsenate on/from Mg–Al layered double hydroxides: Influence of phosphate. *J. Colloid Interface Sci.* **2009**, *333*, 63–70. [CrossRef] [PubMed]
36. Millange, F.; Walton, R.I.; O'Hare, D. Time–resolved *in situ* X–ray diffraction study of the liquid–phase reconstruction of Mg–Al–carbonate hydrotalcite–like compounds. *J. Mater Chem.* **2000**, *10*, 1713–1720. [CrossRef]
37. Nethravathi, C.; Viswanath, B.; Sebastian, M.; Rajamathi, M. Exfoliation of α–hydroxides of nickel and cobalt in water. *J. Colloid Interface Sci.* **2010**, *345*, 109–115. [CrossRef] [PubMed]
38. Herrero, M.; Benito, P.; Labajos, F.M.; Rives, V. Nanosize cobalt oxide–containing catalysts obtained through microwave–assisted methods. *Catal. Today* **2007**, *128*, 129–137. [CrossRef]
39. Panda, H.S.; Srivastava, R.; Bahadur, D. Stacking of lamellae in Mg/Al hydrotalcites: effect of metal ion concentrations on morphology. *Mater Res. Bull.* **2008**, *43*, 1448–1455. [CrossRef]
40. Ye, L.; Zhang, Y.; Wang, S.; Gao, G.; Liu, J.; Zhou, Y.; Liu, H. Synergistic effects and mechanism of $ZnCl_2$ on intumescent flame-retardant polypropylene. *J. Therm. Anal. Calorim.* **2013**, *115*, 1065–1071. [CrossRef]
41. Lee, J.H.; Rhee, S.W.; Jung, D.Y. Ion-exchange reactions and photothermal patterning of monolayer assembled polyacrylate-layered double hydroxide nanocomposites on solid substrates. *Chem. Mater.* **2006**, *18*, 4740–4746. [CrossRef]
42. Wang, L.; Li, B.; Chen, C.; Jia, L. Structural characterization and related properties of the stearate anions intercalated Ni–Al hydrotalcite-like compound prepared by the microwave crystallization. *J. Alloys Compd.* **2010**, *508*, 426–432. [CrossRef]
43. Costache, M.C.; Jiang, D.D.; Wilkie, C.A. Thermal degradation of ethylene–vinyl acetate copolymer nanocomposites. *Polymer.* **2005**, *46*, 6947–6958. [CrossRef]
44. Wang, L.; Sánchez-Soto, M.; Maspoch, M.L. Polymer/clay aerogel composites with flame retardant agents:Mechanical, thermal and fire behavior. *Mater. Des.* **2013**, *52*, 609–114. [CrossRef]